PNAS RESEARCH ARTICLE | IMMUNOLOGY AND INFLAMMATION

Targeted delivery of an anti-inflammatory corticosteroid to Ly6C/G-positive cells abates severity of influenza A symptoms

Novalia Pishesha[a,b,1], Thibault Harmand[a,1], Claire Carpenet[a,1], Xin Liu[a,1], Atul Bhan[c], Ashraful Islam[a], Renate van den Doel[a], William Pinney III[a], and Hidde L. Ploegh[a,2]

Contributed by Hidde Ploegh; received June 27, 2022; accepted September 20, 2022; reviewed by Rino Rappuoli and Vishva Dixit

The distribution of Ly6C/G-positive cells in response to an infection of the mouse respiratory tract with influenza A virus was followed noninvasively over time by immuno-positron emission tomography. We converted nanobodies that recognize Ly6C and Ly6G, markers of neutrophils and other myeloid cells, as well as an influenza hemagglutinin–specific nanobody, into ^{89}Zr-labeled PEGylated positron emission tomography (PET) imaging agents. The PET images showed strong accumulation of these imaging agents in the lungs of infected mice. Immunohistochemistry of influenza virus–infected mice and control mice, injected with a biotinylated and PEGylated version of the Ly6C/G-specific nanobody, showed the presence of abundant Ly6C/G-positive myeloid cells and positivity for Ly6C/G on bronchial epithelium in influenza virus–infected mice. This is consistent with focal inflammation in the lungs, a finding that correlated well with the immuno-PET results. No such signals were detected in control mice. Having shown by PET the accumulation of the Ly6C/G-specific nanobody in infected lungs, we synthesized conjugates of Ly6C/G-specific nanobodies with dexamethasone to enable targeted delivery of this immunosuppressive corticosteroid to sites of inflammation. Such conjugates reduced the weight loss that accompanies infection, while the equivalent amount of free dexamethasone was without effect. Nanobody-drug conjugates thus enable delivery of drugs to particular cell types at the appropriate anatomic site(s). By avoiding systemic exposure to free dexamethasone, this strategy minimizes its undesirable side effects because of the much lower effective dose of the nanobody-dexamethasone conjugate. The ability to selectively target inflammatory cells may find application in the treatment of other infections or other immune-mediated diseases.

nanobody | drug conjugates | neutrophils | PET imaging | inflammation

Significance

Viruses that target the respiratory tract can inflict pulmonary damage, with acute respiratory distress syndrome (ARDS) as a potentially fatal outcome. Neutrophils are key actors in ARDS. Here, we use nanobodies that target Ly6C/G, markers of neutrophils, to image inflammation in the lung and to selectively deliver dexamethasone to the targeted cell population via a nanobody-drug conjugate (NDC) in influenza virus–infected mice. The positron emission tomography imaging data show a clear increase of the Ly6C/G-positive population in the lungs during infection. The NDC prevented weight loss in mice, using but a fraction of the amount of free drug that would be required for treatment.

Viruses that target the respiratory tract can inflict pulmonary damage, with acute respiratory distress syndrome (ARDS) as a potentially fatal outcome. Vaccines that cover the seasonal outbreaks of influenza are only moderately effective and do not afford full protection against such serious outcomes. Infection with influenza virus, even in vaccinated individuals, thus continues to cause morbidity and mortality. In infants, infection of the lower respiratory tract with respiratory syncytial virus can result in ARDS with significant associated mortality. Likewise, the COVID-19 pandemic shows that patients with ARDS may require mechanical ventilatory support and need intensive care (1). Even fully vaccinated individuals are not immune to breakthrough infections with SARS-CoV-2, as evident from recent surges in infections with SARS-CoV-2 variants.

A better understanding of the cells and molecules that contribute to pathology would be therapeutically relevant and benefit from accurate in vivo diagnostic methods. Although the underlying causes of ARDS are not always known and may be diverse, there is consensus about a critical role of activated neutrophils and their products, including neutrophil DNA–containing extracellular traps (NETs) (2–4). Damage inflicted on pneumocytes and lung endothelial cells in the course of virus infection allows secondary infections with opportunistic microorganisms such as *Staphylococcus aureus* to gain a foothold. This, in turn, can lead to an amplification of the neutrophil activation cascade, the formation of NETs, and exacerbation of a cytokine storm, causing yet further damage (5, 6). Combined, these factors contribute to the pathology of serious respiratory tract infections. Treatments that target the relevant cells are therefore actively sought (7–9).

Corticosteroids, and dexamethasone (DEX) in particular, have been used to treat pneumonia and influenza-related ARDS (10–12). DEX treatment has also benefited patients with COVID-19 (13). However, the use of corticosteroids comes with several side effects, some potentially serious. The administration of corticosteroids can affect

Author affiliations: [a]Program in Cellular and Molecular Medicine, Boston Children's Hospital, Harvard Medical School, Boston, MA 02115; [b]Society of Fellows, Harvard University, Cambridge, MA 02138; and [c]Massachusetts General Hospital, Boston, MA 02114

Author contributions: N.P., T.H., X.L., A.B., and H.L.P. designed research; N.P., T.H., C.C., X.L., A.I., R.v.d.D., and W.P. performed research; N.P., T.H., C.C., X.L., and A.I. contributed new reagents/analytic tools; N.P., T.H., C.C., X.L., and A.B. analyzed data; and N.P., T.H., and H.L.P. wrote the paper.

Reviewers: R.R., Toscana Life Sciences Foundation; and V.M.D., Genentech.

Competing interest statement: The authors declare competing interests. N.P. and T.H. are employees of Cerberus Therapeutics; N.P., T.H., and H.L.P. own stock in Cerberus Therapeutics. The remaining authors declare no competing interest.

[1]N.P., T.H., C.C., and X.L. contributed equally to this work.

[2]To whom correspondence may be addressed. Email: Hidde.ploegh@childrens.harvard.edu.

This article contains supporting information online at http://www.pnas.org/lookup/suppl/doi:10.1073/pnas.2211065119/-/DCSupplemental.

Published October 17, 2022.

mental state (14), cause bone fragility (15), and elevate blood sugar levels (16). The latter is of particular concern, as comorbidities such as diabetes predispose to the more severe forms of COVID-19 and complicate treatment with DEX (17). Alternative approaches to treat patients with ARDS are therefore necessary. It would be helpful to have noninvasive imaging tools that can assess the state and location of inflammation as well as the cell types involved. The pioneering work of Ueki et al. recorded the influx of neutrophils and their migratory characteristics at high resolution in an influenza virus–infection model, using two-photon intravital imaging of lung tissue, a method that involves invasive surgery (18). The volume captured in the course of intravital microscopy is limited, with a maximum achievable observation depth of ∼70 μm. While this sophisticated method enables the observation of influenza virus–infected lungs for >4 h during the acute phase of the inflammation and ∼1 h in the lethal phase, it does not allow observations over a period of several days, as the infection and the host response against it run their course, nor can it capture the entire lung (18). Most other methods fail to capture the infected mouse in its entirety.

We have developed two nanobodies—VHH16 and VHH21—that target markers present on granulocytes and other myeloid cells, including neutrophils Ly6C and Ly6G (19). Ly6C and Ly6G are glycosylphosphatidylinositol-anchored membrane proteins that belong to a family of >20 homologous proteins. Members of the Ly6 family may modulate interaction with components of the extracellular matrix and regulate uptake of apoptotic cells by macrophages (20). As evidence for the specificity of VHH16 and VHH21, we found that Ly6C- and Ly6G-negative cells, when transfected with Ly6C or Ly6G complementary DNAs, are recognized by VHH16 and VHH21, with the latter showing stronger binding (19). Even so, given the extent of sequence similarity of Ly6C and Ly6G with other members of the Ly6 family, we cannot exclude the possibility that other Ly6 family members cross-react with VHH16 or VHH21. Immunotoxins based on fusions of VHH16 and VHH21 with *Pseudomonas* exotoxin A, executed using a sortase reaction, deplete granulocyte populations in vivo (19). Ly6C and Ly6G are used as markers for myeloid cells and neutrophils, but the precise function(s) of the Ly6C and Ly6G proteins remain(s) obscure. Ly6C is induced upon exposure to IFN-γ. Of note, its expression is not limited to myeloid cells, because endothelial cells can be induced to express Ly6C as well (21). Remodeling of airway epithelia in response to an infectious event may co-opt interactions of Ly6 family members with extracellular matrix components as part of a protective response or the process of tissue repair.

We hypothesized that the installation of a positron emission tomography (PET) radiotracer on VHH21 should allow noninvasive imaging of the Ly6C/G-positive cell populations in the lungs over the course of a respiratory tract infection. We show that this, indeed, is possible. Furthermore, we surmised that selective delivery of DEX to Ly6C/G-positive cells as a nanobody-drug conjugate would permit a reduction of both the dose and the attendant side effects of corticosteroids, while retaining their bioactive properties (22). We show that the weight loss that accompanies an acute infection with influenza A virus in mice can be abated to a large extent through targeted delivery of DEX to Ly6C/G-positive cells. These cells include myeloid cells as well as bronchial epithelial cells, but only in the lungs of influenza virus–infected mice. The delivered dose of DEX in the form of these conjugates is but a fraction of the amount of free drug that would be required for treatment.

Results

In Vivo Probing Ly6C/G-Positive Cells in an Influenza Virus Infection Model by Immunohistochemistry. The characterization of VHH16 and VHH21 by cytofluorimetry has been reported (19). We generated VHH16 and VHH21 with a C-terminal sortase recognition sequence to site-specifically modify them with fluorophores, biotin, or other substituents. We previously used a labeled version of VHH21 to stain endothelial cells of mouse brain capillaries in the hippocampus (23).

For immunohistochemistry, we engineered monobiotinylated versions of VHH21 by a sortase-mediated conjugation, followed by a click chemistry reaction to attach a 20-kDa polyethylene glycol (PEG20) moiety (Fig. 1 *A* and *B*). The addition of the PEG20 moiety slows clearance of the nanobody construct and reduces kidney retention (24). We have previously shown the suitability and superior tissue penetration of nanobodies compared with full-sized immunoglobulins in immunohistochemical applications (23). For all of the infections with influenza A virus, we used the mouse-adapted human influenza A/WSN/1933 (H1N1) strain.

Mice infected with influenza A virus and uninfected controls received VHH21–biotin–PEG20 intravenously on day 5 postinfection and were killed 24 h later (Fig. 1*C*). Weight loss was used as an indicator of a productive infection. Lungs were harvested and processed for immunohistochemistry. For detection of VHH21–biotin–PEG20, we used streptavidin–horseradish peroxidase and a hematoxylin and eosin counterstain. In the lungs of control mice, we observed a few scattered VHH21-positive cells, whereas the lungs from infected mice showed intense staining of numerous VHH21-positive cells throughout the lung in the alveolar septa (Fig. 1*D*). These cells most likely represent inflammatory cells—findings consistent with interstitial pneumonitis. We also observed staining of the bronchial epithelium, while an arterial branch next to the bronchi did not show endothelial staining. There are also a few Ly6C/G-positive cells in the alveoli. Comparable sections of uninfected lungs were devoid of Ly6C/G positivity (Fig. 1*D*). Our results thus suggest that Ly6C/G-positive cells are recruited to the inflamed lung, and that expression of Ly6C/G is induced in response to inflammation, not only on myeloid and select endothelial cells (21) but also on bronchial epithelium. The inflammatory environment generated during the virus infection induces expression of Ly6C/G, in agreement with data that report strong up-regulation of Ly6C on myeloid cells in response to IFN-γ (21). From these experiments and based on published data, expression of Ly6C/G is obviously not confined to neutrophils.

Dynamic Ly6C/G-Positive Cell Tracing in an Influenza Virus Infection Model by Noninvasive Immune-PET Imaging. To extend our observations on fixed samples to an in vivo setting, we used PET as a noninvasive imaging approach. We have performed PET imaging studies using nanobodies in several mouse models (24–26). We attached to VHH21 a chemical entity bearing an azido group as well as the metal chelator deferoxamine to allow complex formation with radioactive zirconium (^{89}Zr). After its conjugation to VHH21, we exploited the azide moiety to attach a PEG20 molecule via a copper-free click reaction (Fig. 2*A*). Reactions were monitored by sodium dodecyl sulfate–polyacrylamide gel electrophoresis (SDS-PAGE) and liquid chromatography–mass spectrometry (LC-MS) (Fig. 2*B*). The addition of the PEG20 moiety slows clearance of the nanobody construct, reduces kidney retention, and produces better PET

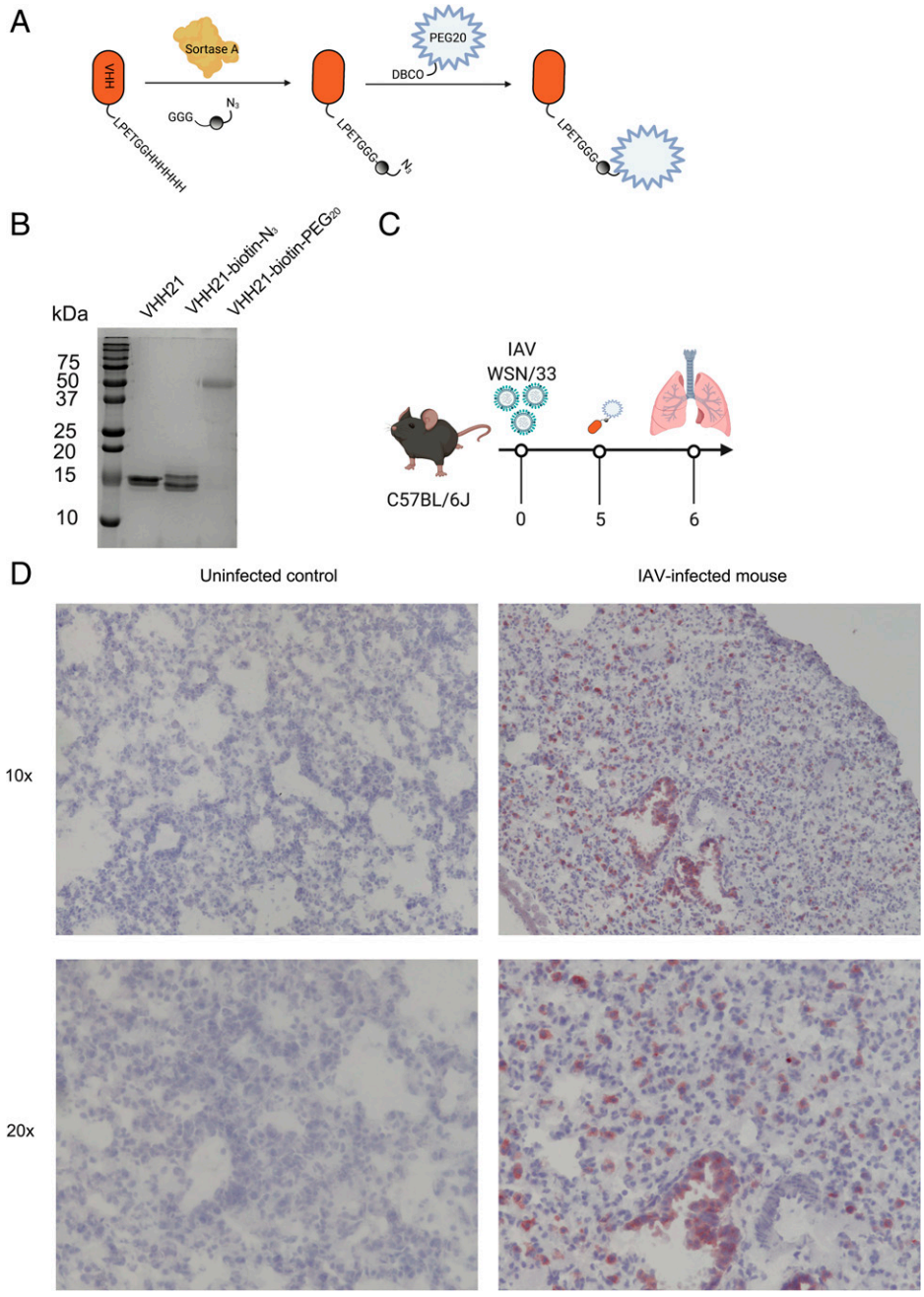

Fig. 1. VHH21 binds to Ly6G/C-positive cells in an influenza virus–infected lung. (*A*) Schematic of site-specific conjugation of VHH21 with biotin-azide using sortase, followed by a PEGylation step. (*B*) The installation of PEG20 affects binding of SDS to the modified protein and is responsible for its heterogenous migration on SDS-PAGE. (*C*) Schematic showing the experimental outline. (*D*) Immunohistochemistry of uninfected and virus-infected lung sections at 10× and 20× magnification. IAV, influenza A virus.

images for several of the nanobodies we have tested (24–26). The imaging agent is referred to hereafter as ^{89}Zr-VHH21.

We used ^{89}Zr-VHH21 to examine by immuno-PET a cohort of mice with different degrees of weight loss, ranging from no weight loss (uninfected controls) to a weight loss of 25% (infected mice) (Fig. 3 *A* and *B*). The extent of weight loss correlates with the severity of the virus infection. We imaged influenza virus–infected animals as well as uninfected controls at 1 h, 24 h, 48 h, and 72h after injection of ^{89}Zr-VHH21 (Fig. 3 *C* and *D*). For the images collected at 1 h postinjection, much of the label remained in the circulation, as evident from a prominent signal in the aortic arches and the heart. This signal decayed over time, owing to the short circulatory half-life of the imaging agent. The PET/computed tomography (CT) images of infected mice and their controls showed a clear difference. There was a strong correlation between the intensity of the ^{89}Zr-VHH21 signal in the lungs and the extent of weight loss: the greater the weight loss, the stronger the ^{89}Zr-VHH21 signal (Fig. 3 *C* and *D* and *SI Appendix*, Fig. S1). Some signal was detected for ^{89}Zr-VHH21 in the lungs of uninfected mice, but this signal was far less intense than in infected mice.

A comparison of the distribution of signal in infected mice at the different time points showed no major regional shifts in the distribution of the ^{89}Zr-VHH21 signal at the spatial resolution afforded by our PET/CT instrument. At the 72-h time point, radioisotope decay contributed to a loss of signal, compounded by the dissociation of ^{89}Zr-VHH21 from its targets in the lung. Any dissociated imaging agent is eliminated via the kidneys or

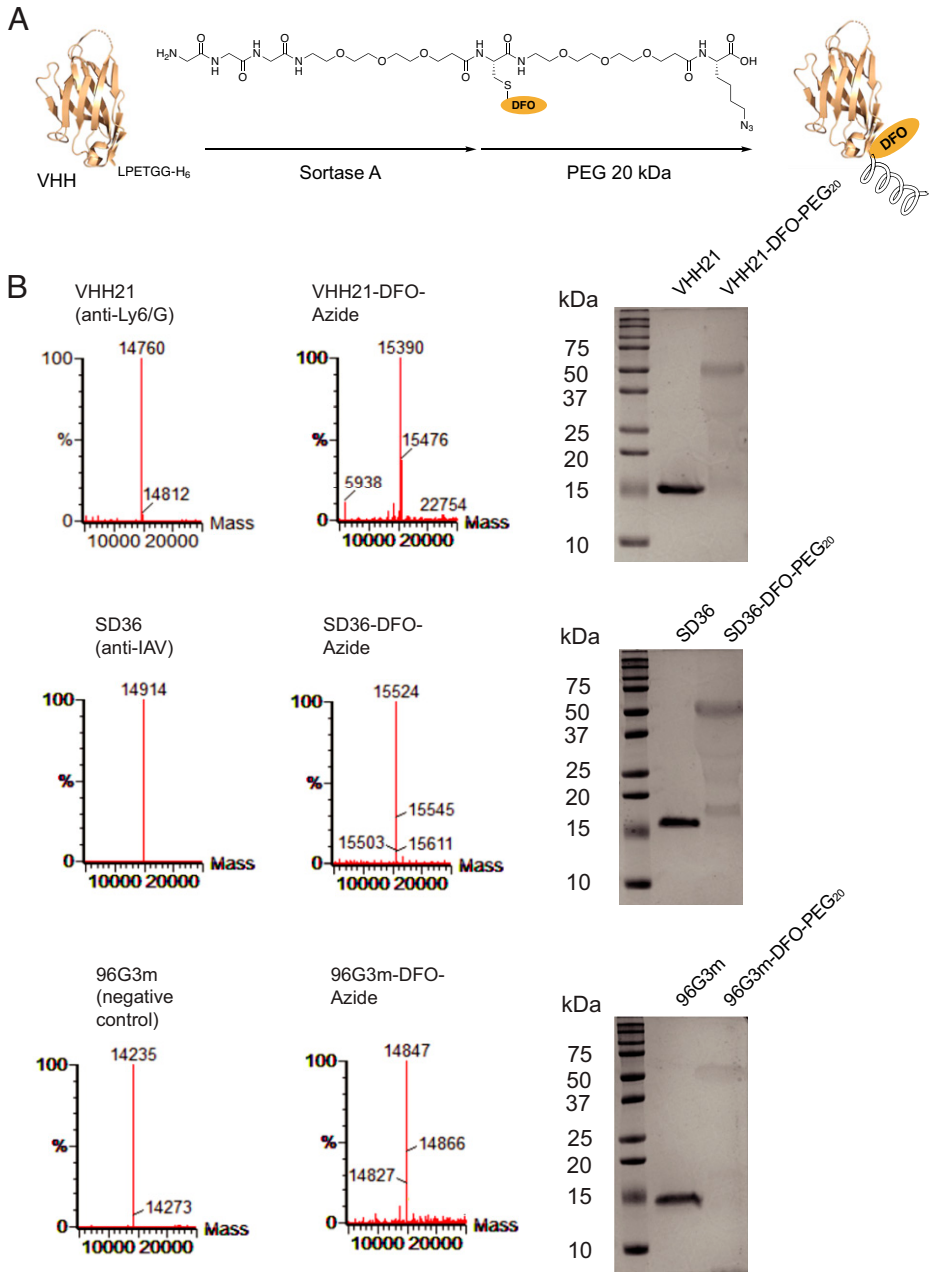

Fig. 2. Characterization of ^{89}Zr-labeled VHHs. (*A*) Schematic representation of ^{89}Zr-labeling and PEGylation of VHHs. (*B*) LC-MS and SDS-PAGE show the purified and modified versions of the indicated VHHs. The installation of PEG20 affects binding of SDS to the modified protein and is responsible for its heterogenous migration on SDS-PAGE. DFO, deferoxamine; IAV, influenza A virus.

can bind to other available targets, either those that are nearby or that can be reached via the circulation. This could account for the relative increase in the ^{89}Zr-VHH21 signal in the spleen, compared with the VHH21 signal in the lung at the 24- and 72-h time points (Fig. 3 *C* and *D*). We conclude that the ^{89}Zr-VHH21 imaging agent can detect the accumulation of Ly6C/G-positive myeloid cells in the lungs and the induction of Ly6C/G on bronchial epithelium that accompany an infection with influenza virus, consistent with the data from immunohistochemistry.

To document the presence of an established influenza virus infection, other than by weight loss and the recruitment of Ly6C/G-positive cells to the lungs of infected mice, we converted an anti-influenza hemagglutinin nanobody, SD36, into an ^{89}Zr-labeled imaging agent, using an approach identical to that used for VHH21 (Fig. 2*B*). The SD36 nanobody recognizes the hemagglutinin of influenza A strains and was thus considered an appropriate imaging agent for these experiments (27). The images obtained with ^{89}Zr single variable domain on a heavy chain (VHH) SD36 for virus-infected mice are very similar to those obtained with ^{89}Zr-VHH21 (Fig. 3 *C* and *D*). A comparison of uninfected controls and virus-infected mice that experienced 22–23% weight loss showed a strong signal for ^{89}Zr-SD36 in the lungs of infected mice, whereas control mice showed accumulation of tracer in liver, bladder, and kidneys, the usual organs of elimination and nonspecific accumulation of label. Consistent with the focal nature of the virus infection, cytokine production would likewise be localized and not homogeneously distributed throughout the lung, thus accounting for the variegated positivity for Ly6C/G of bronchial epithelial structures as seen by immunohistochemistry.

The specificity of nanobodies labeled with PET isotopes is usually addressed in two ways. Competition for accumulation

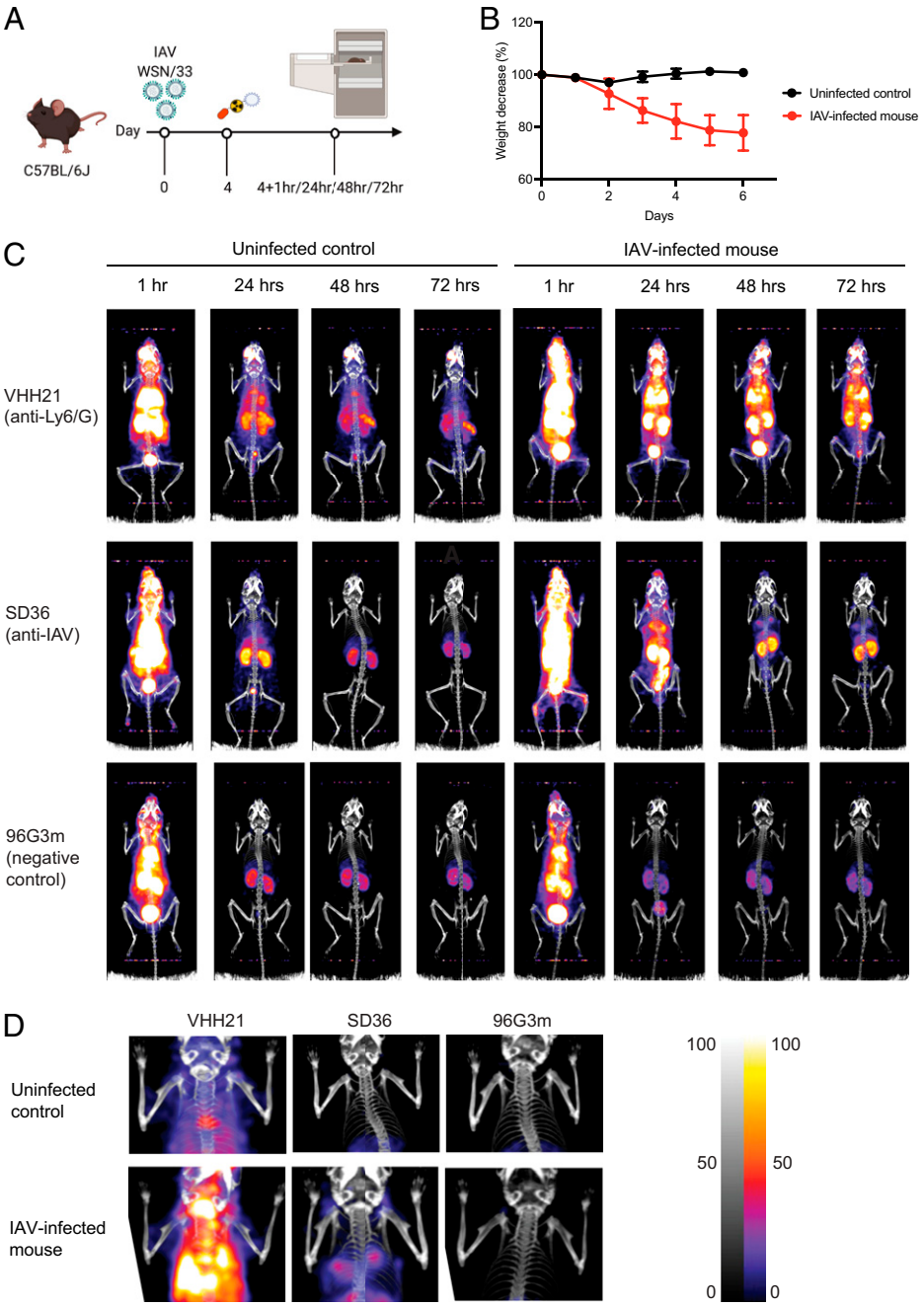

Fig. 3. Ly6C/G-positive cells accumulate in the lung, and their presence correlates with weight loss and virus burden in the lung. (*A*) Schematic showing the experimental outline. (*B*) Graphs showing the percent weight-loss progression after influenza A virus (IAV) infection. (*C*) Representative (n = 3) immune-PET images of IAV-infected mice injected with ^{89}Zr-VHH21, ^{89}Zr-SD36, and ^{89}Zr-96G3m at the indicated time points. (*D*) Images focused on the upper thoracic region (lungs) from (*C*) at the 48-h time point. Scale at *Right* indicates least intense signal to most intense.

of label by injection of a large bolus of unlabeled imaging agent prior to injection of the radiolabeled imaging agent is commonly used to adduce specificity of the signal. A more rigorous approach is to use mice that are genetically deficient in the marker targeted by the imaging agent, for example PD-L1–deficient and proficient mice, imaged with anti–PD-L1 VHH (28), or to use mice that lack the target cell population altogether, for example, RAG-deficient (which lack mature lymphocytes) and RAG-proficient mice, imaged with an ^{89}Zr-labeled, PEGylated anti-CD8 VHH (24). A comparison of influenza virus–infected mice and uninfected controls, as we have done here for ^{89}Zr-SD36, approximates that situation but fails to consider changes in hemodynamics and perfusion in the infected lung as possible confounding factors. We therefore used as a specificity control an ^{89}Zr-labeled VHH (96G3m) that lacks a target in mice (Fig. 2*B*). Infected and control mice yield indistinguishable patterns of labeling with this irrelevant VHH 96G3m (Fig. 3 *C* and *D*), thus attesting to the specificity of the ^{89}Zr-VHH21 and ^{89}Zr-SD36 signals.

Targeted Delivery of DEX to Ly6C/G+ Cells Ameliorates Symptoms in an Influenza Virus–Infected Mouse Model. We can selectively deliver DEX to cells of interest through the creation of nanobody-drug adducts (22, 29). The approach relies on site-specific attachment of a drug, in this case DEX, to the desired nanobody via a hydrazone-based linker. This linker, cleaved at acidic pH, releases DEX inside the cell upon endocytosis of the VHH–drug conjugate. The synthetic approach used

to obtain the DEX adduct was designed such that other anti-inflammatory steroids with an accessible ketone function could be installed using the same strategy. Having established the ability of neutrophil-specific VHHs to target neutrophils in vivo by immuno-PET, we synthesized VHH–DEX adducts.

Given the accumulation of Ly6C/G positivity in the lungs of mice infected with influenza virus, we hypothesized that targeted suppression of inflammation by DEX might be an attractive means of reducing the pathological consequences of a respiratory tract infection. We thus equipped VHH16 and VHH21 with a single DEX molecule using sortase A (Fig. 4*A*), a ligation that proceeds smoothly. Both constructs were obtained and characterized without difficulty. Two injections of the VHH-DEX adduct, each delivering 500 ng of DEX per injection, significantly reduced weight loss in virus-infected mice, whereas two injections of free DEX, at 500 ng each (equivalent to ~25 μg/kg), did not provide any protection against weight loss (Fig. 4*B*). As a comparison, during the COVID-19 pandemic, the RECOVERY (Randomized Evaluation of COVID-19 Therapy) trial (ClinicalTrials.gov identifier NCT04381936) used a dose of 6 mg/d/patient over 10 d (~80 μg/kg/d for an ~75-kg patient) (13). The DEX-ARDS (Efficacy Study of Dexamethasone to Treat the Acute Respiratory Distress Syndrome) and CoDEX (COVID-19–Associated ARDS

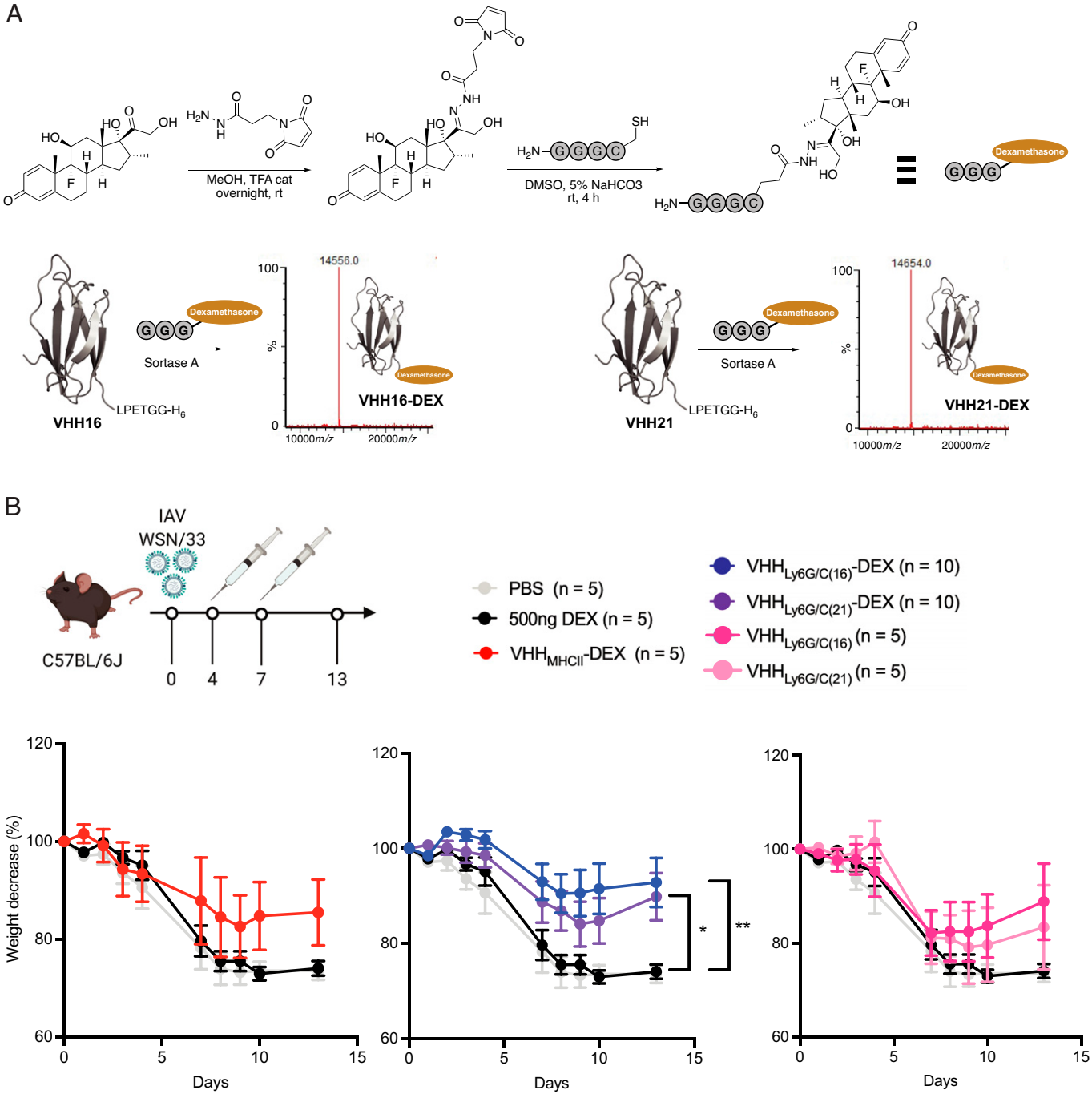

Fig. 4. Delivery of DEX by anti–Ly6C/G-positive VHHs reduces severity of symptoms in influenza A virus (IAV)–infected mice. (*A*) Schematic depicting the synthesis of GGGC-DEX and the LC-MS profiles to confirm the purity of VHH-DEX adducts. (*B*) Schematic showing the experimental outline and graphs showing the percent weight loss post-IAV infection in mice that received the different treatments as indicated. The data represent mean ± SEM of biological replicates (n = 5–10 as indicated in the legend). *P < 0.05, **P < 0.01 (two-way ANOVA with repeated measures). rt, room temperature; TFA, trifluoroacetic acid; cat, catalytic amount.

Treated with Dexamethasone: Alliance COVID-19 Brasil III) trials (ClinicalTrials.gov identifiers NCT01731795 and NCT04327401, respectively) used a dose of 20 mg/d/patient (~270 μg/kg/d for an ~75-kg patient) for 5 d and 10 mg/d/patient (~135 μg/kg/d for an ~75-kg patient) for 5 additional days (30, 31). Immunotoxins based on VHH16 appeared to be more effective at neutrophil depletion in vivo than those based on VHH21 (Fig. 4*B*) (19). While preliminary data using flow cytometry showed better binding for VHH21, we decided to use the difference in efficacy of these two VHHs and combine them in a treatment and imaging experiment with the VHH16-DEX as the therapeutic entity and VHH21 for the construction of the imaging agent.

Mice were infected with influenza A and, on day 4 postinfection, received VHH16-DEX or phosphate-buffered saline (PBS) intravenously. Weight loss was recorded and, on day 5, the imaging sequence was started. Mice were imaged for the subsequent 3 d (*SI Appendix*, Fig. S2). We observed a clear difference in weight loss between mice treated with PBS and mice treated with VHH16-DEX. Mice treated with VHH16-DEX in the imaging cohort started to lose weight on day 6 (*SI Appendix*, Fig. S2). To avoid multiple rounds of anesthesia, these mice received only a single dose of VHH16-DEX, as subsequent days were reserved for imaging experiments.

Discussion

The PET images of the lungs of influenza virus–infected mice, imaged with ^{89}Zr-VHH21, were comparable for mice treated with VHH16-DEX or PBS. Although VHH16-DEX reduced weight loss in infected mice, it did not affect the distribution of the PET signal. We are not aware of other studies that tracked an inflammatory response over time in live mice by visualization of participating cells. DEX is known to reduce NETosis of neutrophils (32, 33) and down-regulate the release of inflammatory molecules (34). This might suffice to blunt inflammation through a reduction of the number of neutrophils and their products at the site(s) of infection. There are at least two processes that can serve as the target for inhibition by DEX. The influx of Ly6C/G-positive cells includes macrophages and neutrophils, which may be targeted by the drug. Second, the infection induces strong positivity for VHH21 on bronchial epithelial cells (Fig. 1*C*), a nonmigratory cell type. We interpret such induction of Ly6C/G positivity as evidence of local exposure to proinflammatory cytokines. Without having identified the actual cell type responsible for local synthesis and release of such cytokines, targeted delivery of an inhibitory anti-Ly6C/G VHH-DEX adduct should blunt the ensuing inflammatory response at those sites. The detection of Ly6C/G on cell types other than neutrophils or other myeloid cells is perhaps best illustrated by its presence on bronchial epithelial cells, an unexpected observation. The extent to which targeted delivery of DEX to a broader population of cells is essential to observe its anti-inflammatory effects is difficult to establish in the face of Ly6C/G's expression pattern. However, we favor the involvement of neutrophils, given their role in the inflammatory process. The recruitment of scattered cells of a morphology consistent with that of neutrophils is due to recruitment of such cells to sites of inflammation. Recruitment of neutrophils is known to occur rapidly upon receipt of an inflammatory stimulus such as tissue damage (35). In contrast, the detection of Ly6C/G on bronchial epithelial cells must be caused by induction of expression on these cells, given the time point at which we observed Ly6C/G positivity.

From a translational perspective, we consider the synthesis of nanobody–DEX adducts particularly appealing: they allow targeted delivery of this anti-inflammatory payload, thus affording reductions of the administered dose by some 200-fold, compared with free DEX (22). In the present study, the administered dose of 25 μg/kg/d is far lower than that commonly used for free DEX (1 to 4 mg/kg/d) to treat respiratory tract infections. The known application of DEX in conditions such as ARDS and the dose reduction achieved in this study by targeted delivery of DEX to inflammatory cells thus suggest the therapeutic potential of nanobody–drug adducts. The short circulatory half-life of these adducts, which could be considered a drawback from a pharmacokinetic perspective, may in fact be an asset, as it reduces systemic drug exposure in case the linker via which the drug is attached is cleaved in the circulation. The small size of nanobody–drug adducts also improves their tissue penetration.

Furthermore, our immuno-PET and immunofluorescence data show that the dwell time of such adducts on the intended target cell population can be much longer than the circulatory levels of these modified nanobodies would suggest. A nanobody that dissociates from its target on a tissue-resident cell is far more likely to rebind to that same (or an adjacent) cell than to be diluted in extracellular fluid and swept away, for example, by lymphatic flow. The affinity of the nanobody for its target, the number and local density of accessible target molecules per cell, and the efficiency with which the tissue where the target cell resides is perfused are all variables that will determine dwell time of the labeled nanobody on cells of interest.

In conclusion, nanobody-based PET imaging can detect inflammation that accompanies infectious disease and inspire new methods of treatment. Immuno-PET lacks the high spatial and temporal resolution of intravital microscopy, but it has the singular advantage of being noninvasive, enabling tracking the intact living animal over a period of days (25, 36, 37). It thus allows observation windows that better match the kinetics of a virus infection and the immune response against it. Imaging agents that detect the presence of viral antigens, such as the SD36 anti-influenza hemagglutinin nanobody, or that recognize Ly6C/G-positive cells provide a window on infection of the respiratory tract. Through correlation of immunohistochemical results with the PET images, both obtained with a Ly6C/G-specific nanobody, new forms of treatment may be envisaged.

Materials and Methods

Expression of VHHs and Endotoxin Removal. WK6 *E. coli* containing the plasmid encoding VHHs were grown to midlog phase at 37 °C in Terrific Broth plus ampicillin and induced with 1 mM isopropyl β-D-1-thiogalactopyranoside overnight at 30 °C. Bacteria were harvested by centrifugation at 5,000*g* for 15 min at 4 °C and then resuspended in 25 mL 1× TES buffer (200 mM Tris, pH 8, 0.65 mM EDTA, 0.5 M sucrose) per liter of culture and incubated for 1 h at 4 °C with agitation. Resuspended cells were then submitted to osmotic shock by 1:4 dilution in 0.25× TES buffer and incubation overnight at 4 °C. The periplasmic fraction was isolated by centrifugation at 5,000*g* for 30 min at 4 °C and then loaded onto Ni-NTA (Qiagen) in 50 mM Tris, pH 8, 150 mM NaCl, and 10 mM imidazole. Protein was eluted in 50 mM Tris, pH 8, 150 mM NaCl, 500 mM imidazole, and 10% glycerol and then loaded onto a Superdex 75 10/300 column in 50 mM Tris, pH 8, 150 mM NaCl, and 10% glycerol. The peak fractions were recovered and rebound to Ni-NTA for depletion of lipopolysaccharide (<2 IU/mg). Bound VHHs were washed with 40 column volumes of PBS + 0.1% TritonX-114 and eluted in 2.5 column volumes of endotoxin-free PBS (Teknova) with 500 mM imidazole. Imidazole was removed by size exclusion on a PD10 column (GE Healthcare) and elution in lipopolysaccharide-free PBS. Purity of recombinant VHHs was assessed by SDS-PAGE and LC-MS.

Synthesis of Peptides. Peptides were synthesized on 2-chlorotrityl resin (ChemImpex) following standard solid-phase peptide synthesis protocols or were obtained commercially from GenScript.

Peptide GGGC and GGGK(azide) with a free N terminus and a C-terminal amide were synthesized following standard solid-phase synthesis protocols. All fluorenylmethyloxycarbonyl (Fmoc) amino acids were purchased from Chempep, Inc. Fmoc-Lys(azide)-OH was used as a building block to provide the bio-orthogonal handle. Peptides were purified by reverse-phase high-performance liquid chromatography (HPLC). Their identity was confirmed by LC-MS prior to deferoxamine maleimide coupling to the cysteine-free thiol. Peptides were further purified by reverse-phase HPLC. Their identity was confirmed by LC-MS.

To obtain GGGC–DEX, DEX (Sigma Aldrich; 25 mg, 64 μmol) and *N*-β-maleimidopropionic acid hydrazide (ThermoFisher; 40 mg, 135 μmol) were dissolved in 3.0 mL of dry MeOH (Sigma Aldrich). One drop of trifluoroacetic acid was added to the solution. The resulting mixture was agitated overnight at room temperature. The solution was taken to dryness and the residue was dissolved in dimethyl sulfoxide (DMSO; 1.0 mL), purified by reverse-phase HPLC, and lyophilized. The resulting powder was stored at −20 °C. The calculated mass for DEX–maleimide ($C_{29}H_{37}FN_3O_7$ [M+H]+) was 558.26, found 558.32. In a second reaction, DEX–maleimide (20 mg, 36 μmol) and GGGC (21 mg, 72 μmol) were dissolved in 5% 0.1 M $NaHCO_3$ in DMSO (1.0 mL). The resulting mixture was agitated at room temperature until completion of the reaction. Once no starting material was left, the reaction mixture was directly purified by reverse-phase HPLC and lyophilized. The mass calculated for GGGC-DEX ($C_{38}H_{53}FN_7O_{12}S$ [M+H]+) was 850.35, found 850.21. The resulting peptide was stored at −20 °C and redissolved in PBS at the desired concentration prior to sortase ligation.

C-terminal Sortagging of VHH-LPETGG with GGG-Carrying Moieties and PEGylation. Ca^{2+}-independent heptamutant (7M) Sortase A derived from *S. aureus* (10 μM final concentration, 10× stock in 50 mM Tris, pH 7.4, 150 mM NaCl) and GGGC-based peptides (0.5 mM final concentration) were added to VHHs (50 μM final concentration) in PBS. The resulting mixture was incubated at 4 °C overnight. After incubation, unreacted VHH and 7M-Sortase A were removed by adsorption onto Ni-NTA agarose beads. The unbound fraction was concentrated, and excess nucleophile was removed using an Amicon 3,000-kDa MWCO filtration unit (Millipore). Reaction products were analyzed by SDS-PAGE and LC-MS to assess purity and stored frozen at −80 °C. PEGylated VHHs were generated by reacting the bio-orthogonal azide group with dibenzocyclooctyne–PEG20 overnight. The end product was analyzed by SDS-PAGE to confirm the efficiency of coupling.

Mice. All animals were housed in the animal facility at Boston Children's Hospital and were maintained according to protocols approved by the Boston Children's Hospital Committee on Animal Care. C57BL/6J ($CD45.2^+$) mice were either purchased from the Jackson Laboratory or bred in-house. Only female mice aged 8 to 12 wk were used in this study.

Infection of Mice with Influenza Virus. Mice were anesthetized with isoflurane and infected by the intranasal route with 4×10^4 infectious units of influenza virus A/WSN/1933 (H1N1) diluted in 20 μL PBS. Control mice were mock infected with an equal volume of PBS. Infection was tracked by monitoring daily weight loss. Mice were euthanized with CO_2 when weight loss exceeded 25% of initial body weight and/or animals displayed signs of severe distress, or if no weight was recovered 9 d postinfection. Unless indicated otherwise, for treatment with VHH–DEX, 20 mg VHH–DEX, an equimolar amount of free DEX only, and equimolar amounts of unmodified VHHs were administered intravenously at days 4 and 7 after influenza virus A infection.

Immunohistochemistry. Lungs from influenza virus–infected and control C57BL/6J ($CD45.2^+$) mice were harvested 24 h post intravenous injection of 100 μg of VHH–Biotin–PEG20k and stored in Tissue Plus O.C.T. compound (Fisher Healthcare) at −80 °C. Frozen sections (10-μm thick) were prepared on a Shandon Cryotome E Cryostat Microtome (Thermo Scientific). Sections were fixed for 20 min in 4% (vol/vol) paraformaldehyde in PBS. Endogenous peroxidase activity was blocked by incubation for 10 min in 0.3% (vol/vol) H_2O_2 in PBS. Sections were then incubated in a humidified chamber at room temperature for 1 h in 3% (wt/vol) bovine serum albumin, 0.05% (vol/vol) Tween 20 in PBS. Streptavidin-horseradish peroxidase (Thermo Scientific) was then added in a humidified chamber for 45 min in the dark. AEC Substrate Kit (BD Pharmingen) was added for 15 min at room temperature in the dark. Slides were counterstained with Mayer's Hematoxylin solution (Sigma-Aldrich) for 2 min and rinsed in running tap water for 10 min. Slides were dried and mounted using Prolong Gold antifade reagent (Molecular Probes) for analysis by microscopy.

Immuno-PET Imaging. PET-CT procedures have been described in detail elsewhere (1). Briefly, mice were anesthetized using 2% isoflurane in O_2 at a flow rate of ∼1 L/min. Mice were imaged with a G8 PET-CT small-animal scanner (PerkinElmer). PET images were acquired over a 10-min period, which was followed by ∼2 min of CT acquisition.

Data Availability. All study data are included in the article and/or supporting information.

ACKNOWLEDGMENTS. This study was supported by a Junior Fellowship from Harvard Society of Fellows (N.P.), The Norwegian Cancer Society (Project 198164), UiT The Arctic University of Norway (A.I.), and the NIH Director's Pioneer Award (grant 1DP1AI150593-01 to H.L.P.).

1. S. Möhlenkamp, H. Thiele, Ventilation of COVID-19 patients in intensive care units. *Herz* **45**, 329–331 (2020).
2. A. Arcanjo *et al.*, The emerging role of neutrophil extracellular traps in severe acute respiratory syndrome coronavirus 2 (COVID-19). *Sci. Rep.* **10**, 19630 (2020).
3. M. Ackermann *et al.*, Patients with COVID-19: In the dark-NETs of neutrophils. *Cell Death Differ.* **28**, 3125–3139 (2021).
4. S.-C. Yang, Y.-F. Tsai, Y.-L. Pan, T.-L. Hwang, Understanding the role of neutrophils in acute respiratory distress syndrome. *Biomed. J.* **44**, 439–446 (2021).
5. C.-E. Luyt *et al.*, Pulmonary infections complicating ARDS. *Intensive Care Med.* **46**, 2168–2183 (2020).
6. P. Manohar *et al.*, Secondary bacterial infections in patients with viral pneumonia. *Front. Med. (Lausanne)* **7**, 420 (2020).
7. C.-C. Chiang, M. Korinek, W.-J. Cheng, T.-L. Hwang, Targeting neutrophils to treat acute respiratory distress syndrome in coronavirus disease. *Front. Pharmacol.* **11**, 572009 (2020).
8. B. J. Barnes *et al.*, Targeting potential drivers of COVID-19: Neutrophil extracellular traps. *J. Exp. Med.* **217**, e20200652 (2020).
9. D. K. Chellappan *et al.*, Targeting neutrophils using novel drug delivery systems in chronic respiratory diseases. *Drug Dev. Res.* **81**, 419–436 (2020).
10. A. Stern *et al.*, Corticosteroids for pneumonia. *Cochrane Database Syst. Rev.* **12**, CD007720 (2017).
11. B. T. Thompson, Corticosteroids for ARDS. *Minerva Anestesiol.* **76**, 441–447 (2010).
12. Y. Zhou *et al.*, Use of corticosteroids in influenza-associated acute respiratory distress syndrome and severe pneumonia: A systemic review and meta-analysis. *Sci. Rep.* **10**, 3044 (2020).
13. P. Horby *et al.*; RECOVERY Collaborative Group, Dexamethasone in hospitalized patients with Covid-19. *N. Engl. J. Med.* **384**, 693–704 (2021).
14. T. P. Warrington, J. M. Bostwick, Psychiatric adverse effects of corticosteroids. *Mayo Clin. Proc.* **81**, 1361–1367 (2006).
15. R. Mitra, Adverse effects of corticosteroids on bone metabolism: A review. *PM R* **3**, 466–471, quiz 471 (2011).
16. J. J. Pasternak, D. G. McGregor, W. L. Lanier, Effect of single-dose dexamethasone on blood glucose concentration in patients undergoing craniotomy. *J. Neurosurg. Anesthesiol.* **16**, 122–125 (2004).
17. J. Alessi, G. B. de Oliveira, B. D. Schaan, G. H. Telo, Dexamethasone in the era of COVID-19: Friend or foe? An essay on the effects of dexamethasone and the potential risks of its inadvertent use in patients with diabetes. *Diabetol. Metab. Syndr.* **12**, 80 (2020).
18. H. Ueki *et al.*, In vivo imaging of the pathophysiological changes and neutrophil dynamics in influenza virus-infected mouse lungs. *Proc. Natl. Acad. Sci. U.S.A.* **115**, E6622–E6629 (2018).
19. C. Bachran *et al.*, The activity of myeloid cell-specific VHH immunotoxins is target-, epitope-, subset- and organ dependent. *Sci. Rep.* **7**, 17916 (2017).
20. P. Y. Lee, J.-X. Wang, E. Parisini, C. C. Dascher, P. A. Nigrovic, Ly6 family proteins in neutrophil biology. *J. Leukoc. Biol.* **94**, 585–594 (2013).
21. M. A. Jutila *et al.*, Ly-6C is a monocyte/macrophage and endothelial cell differentiation antigen regulated by interferon-gamma. *Eur. J. Immunol.* **18**, 1819–1826 (1988).
22. N. Pishesha *et al.*, Induction of antigen-specific tolerance by nanobody-antigen adducts that target class-II major histocompatibility complexes. *Nat. Biomed. Eng.* **5**, 1389–1401 (2021).
23. T. Fang *et al.*, Nanobody immunostaining for correlated light and electron microscopy with preservation of ultrastructure. *Nat. Methods* **15**, 1029–1032 (2018).
24. M. Rashidian *et al.*, Predicting the response to CTLA-4 blockade by longitudinal noninvasive monitoring of CD8 T cells. *J. Exp. Med.* **214**, 2243–2255 (2017).
25. T. J. Harmand, A. Islam, N. Pishesha, H. L. Ploegh, Nanobodies as *in vivo*, non-invasive, imaging agents. *RSC Chem Biol* **2**, 685–701 (2021).
26. A. Islam *et al.*, Converting an anti-mouse CD4 monoclonal antibody into an scFv positron emission tomography imaging agent for longitudinal monitoring of $CD4^+$ T cells. *J. Immunol.* **207**, 1468–1477 (2021).
27. N. S. Laursen *et al.*, Universal protection against influenza infection by a multidomain antibody to influenza hemagglutinin. *Science* **362**, 598–602 (2018).
28. J. R. Ingram *et al.*, PD-L1 is an activation-independent marker of brown adipocytes. *Nat. Commun.* **8**, 647 (2017).
29. T. Fang *et al.*, Structurally defined αMHC-II nanobody-drug conjugates: A therapeutic and imaging system for B-cell lymphoma. *Angew. Chem. Int. Ed. Engl.* **55**, 2416–2420 (2016).
30. J. Villar *et al.*; dexamethasone in ARDS network, Dexamethasone treatment for the acute respiratory distress syndrome: A multicentre, randomised controlled trial. *Lancet Respir. Med.* **8**, 267–276 (2020).

31. B. M. Tomazini *et al.*; COALITION COVID-19 Brazil III Investigators, Effect of dexamethasone on days alive and ventilator-free in patients with moderate or severe acute respiratory distress syndrome and COVID-19: The CoDEX randomized clinical trial. *JAMA* **324**, 1307–1316 (2020).
32. T. Wan, Y. Zhao, F. Fan, R. Hu, X. Jin, Dexamethasone inhibits *S. aureus*-induced neutrophil extracellular pathogen-killing mechanism, possibly through toll-like receptor regulation. *Front. Immunol.* **8**, 60 (2017).
33. M. J. Lapponi *et al.*, Regulation of neutrophil extracellular trap formation by anti-inflammatory drugs. *J. Pharmacol. Exp. Ther.* **345**, 430–437 (2013).
34. S. Sinha *et al.*, Dexamethasone modulates immature neutrophils and interferon programming in severe COVID-19. *Nat. Med.* **28**, 201–211 (2022).
35. T. Lämmermann *et al.*, Neutrophil swarms require LTB4 and integrins at sites of cell death in vivo. *Nature* **498**, 371–375 (2013).
36. A. R. Kherlopian *et al.*, A review of imaging techniques for systems biology. *BMC Syst. Biol.* **2**, 74 (2008).
37. Q. Cao *et al.*, PET imaging of acute and chronic inflammation in living mice. *Eur. J. Nucl. Med. Mol. Imaging* **34**, 1832–1842 (2007).